

Reconciling petrologic magma ascent speedometers for the June 12th, 1991 eruption of Mount Pinatubo, Philippines

 Megan Harris*^α,  Behnaz Hosseini^α,  Madison Myers^{†α}, and  Logan Bouley^α

^αDepartment of Earth Sciences, Montana State University, Bozeman, MT 59717, USA.

ABSTRACT

We investigate whether decompression rates derived from three often-disparate petrologic techniques (microlites, bubbles, and melt embayments) can be reconciled or integrated for a more complete understanding of magma ascent in the conduit. We focus on the well-studied and -documented earliest Plinian eruptions (June 12, 1991) of Mount Pinatubo. Using a newly developed two-stage decompression-diffusion model, volatile profiles in quartz-hosted embayments reveal an initial stage of decompression nearly two orders of magnitude slower than final rates. In applying time-integrated models of microlite and bubble nucleation and growth, initial decompression rates from embayments are supported by microlite modeling results, whereas final rates are in close agreement with bubble number densities. This consistency and continuity between speedometers supports the sensitivity of different petrologic recorders to specific regions of the conduit system and highlights the fidelity of embayments as recorders of decompression throughout the entire conduit. Ascent timescales derived from Pinatubo embayments range from hours to days, coinciding with the visual onset of lava effusion leading to explosive activity.

KEYWORDS: Bubbles; Microlites; Embayments; Decompression; Numerical modeling.

1 INTRODUCTION

The path of magma decompression and degassing during ascent exerts a strong control over the nature of an eruption, where fluctuations in internal properties (e.g. viscosity) are thought to control shifts in eruption intensity [e.g. Papale and Polacci 1999; Gonnermann and Manga 2007; Cassidy et al. 2018]. This relationship is largely driven by the behavior of volatiles responding to a decrease in pressure. As magma ascends, the solubility of dissolved volatile species (primarily H₂O and CO₂) decreases, which leads to the exsolution of the volatile species into a fluid phase. Although magma ascent is not the only mechanism by which magma can experience decompression, for erupted materials it is generally assumed that the two processes are coupled. This history of decompression and volatile exsolution is recorded in all three phases of the magma and has commonly been examined for explosive eruptions by measuring 1) the size and abundance of vesicles [e.g. Toramaru 2006; Hamada et al. 2010; Shea et al. 2010], 2) the size and abundance of microlites [e.g. Hammer et al. 1999; Toramaru et al. 2008; Brugger and Hammer 2010; Befus and Andrews 2018], and 3) the volatile gradients [e.g. Liu et al. 2007; Lloyd et al. 2014; Myers et al. 2018; 2021; Saalfeld et al. 2022] (Figure 1A). The formation of bubbles, microlites, and volatile gradients are all modulated by a feedback loop between gas exsolution and magma decompression; however, the kinetics of their respective formations operate on very different timescales [Brandeis and Jaupart 1987; Mangan et al. 1993; Shea 2017; Cassidy et al. 2018]. For instance, although bubble textures inherited from the storage region are susceptible to modification by gas migration and coalescence, a final bubble nucleation event can occur in the shallow conduit such that bubble number densities (BND) often record the final, syn-

eruptive decompression event [Massol and Koyaguchi 2005; Toramaru 2006; Hamada et al. 2010; Hajimirza et al. 2019] (Figure 1A). Thus, compared to other techniques, bubbles may provide information about the latest stage of ascent, where the BND speedometer has classically returned extremely fast decompression rates (Shea [2017]: 1–100 MPa s⁻¹ using the calibration by Toramaru [2006]). On the other end of the resolvable decompression rate spectrum are rates determined from modeling microlite number density (MND). MND is based on compositionally-dependent crystal nucleation and growth rates, triggered by undercooling that drives H₂O loss from the melt, forming crystals relatively slowly (10⁻⁶–10⁻⁹ mm s⁻¹ for plagioclase in silicic melt [Brugger and Hammer 2010]). This technique provides a record of decompression on the order of hours to days (0.0001–0.0006 MPa s⁻¹ [Nicholis and Rutherford 2004; Castro and Gardner 2008; Brugger and Hammer 2010; Armienti et al. 2013]). Therefore, MND is often better suited to recording slower timescales of magma ascent and/or stalling in the conduit system [Hammer et al. 1999] (Figure 1A). Recent studies measuring and modeling volatile gradients preserved in melt embayments have found decompression rates that bridge the gap between the BND and MND methods (0.0001–0.1 MPa s⁻¹ [Myers et al. 2018; Moussallam et al. 2019; Myers et al. 2021; Saalfeld et al. 2022; Befus et al. 2023]), corresponding to timescales of minutes to days. Importantly, all three petrologic methods for estimating magma ascent rates have traditionally assumed a simplified single-step, multi-step, or continuous constant-rate decompression path (Figure 1B). While simplifications are always necessary when modeling natural systems, magma ascent is a non-linear process [Wilson et al. 1980; Mastin 2002], and thus bubble and microlite nucleation and growth, as well as volatile gradients in embayments, must also be modeled with non-linearity in mind (Figure 1B).

*✉ dr.meganharris22@gmail.com

†✉ madison.myers@montana.edu

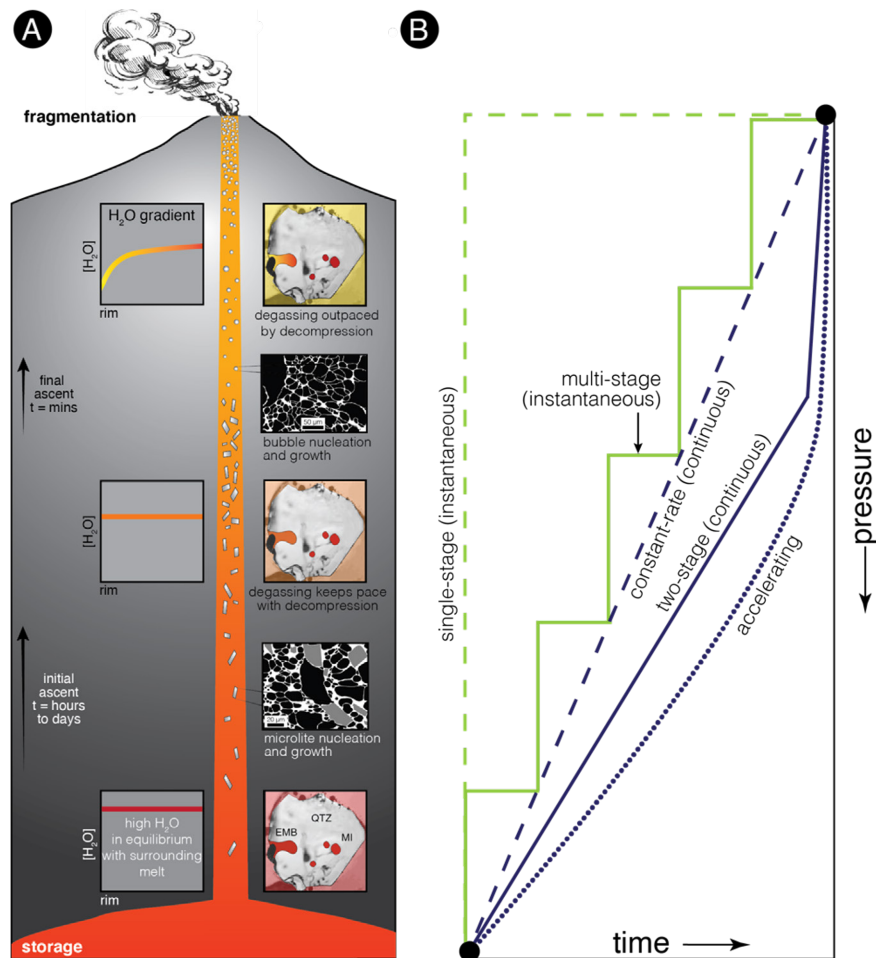


Figure 1: [A] Generalized conduit schematic, illustrating how the H₂O concentration profile along an embayment evolves during decompression. At depth, prior to significant H₂O exsolution, H₂O diffusion through the embayment channel keeps pace with slower decompression. At shallower depths, bubble nucleation and growth drive rapid H₂O exsolution and buoyancy-driven decompression, and H₂O diffusion through the embayment no longer keeps pace, forming a gradient from the interior to the rim. In general, the kinetics of microlite and bubble nucleation and growth are such that microlite textures record slower decompression in the deep conduit, while bubble textures record faster decompression in the shallow conduit. [B] Various magma decompression paths used in ascent rate modeling, including instantaneous decompression paths in green and continuous in blue. Examples of instantaneous decompression pathways are single-stage (dashed green line) and multi-stage (solid green line). Examples of continuous decompression pathways are constant-rate (dashed blue line), two-stage (solid blue line), and accelerating (dotted blue line).

Recent advances in extracting decompression rates from petrologic tools include boundary conditions that more accurately reflect natural systems. For instance, where the original BND modeling approach was skewed toward reproducing decompression rates associated with peak nucleation, the approach by [Hajimirza et al. \[2021\]](#) retrieves a time-averaged decompression rate, accounting for both the decompression pathway associated with the nucleation of bubbles deep in the conduit and the accelerating decompression associated with shallower bubble growth. Using these time-averaged decompression models negates the bias toward faster ascent rates associated with shallow bubble nucleation. A similar effort exists within the MND modeling community. Previous work by [Hammer and Rutherford \[2002\]](#) used single-step decompression and multi-step decompression paths to calculate av-

erage nucleation and growth rates. While this setup provides a good first-order approximation of microlite growth, it does not represent a continuous decompression path but instead simulates instantaneous intrusion and stalling. Modeling along these pathways requires a higher degree of supersaturation than was likely experienced, and thus the system is initially more nucleation-dominated, resulting in an overestimation of decompression rate [[Andrews and Befus 2020](#)]. The program SNGPLag has sought to improve microlite geospeedometry by applying time-integrated nucleation and growth rates based on constant-rate decompression experiments [[Befus and Andrews 2018](#)], allowing for modeling with constant and continuously accelerating decompression pathways, a more likely approximation of natural systems [[Andrews and Befus 2020](#)]. Additionally, unlike previous models, SNGPLag considers the

presence of preexisting phenocrysts and antecrysts, which can facilitate crystal growth during decompression. These additions result in lower degrees of supersaturation in the system and thus fewer microlites due to the reduced nucleation rates [Andrews and Befus 2020]. Finally, while modeling volatile gradients in embayments has proven to be a powerful tool, the current models (e.g. EMBER [Georgeais et al. 2021]; Embayment Diffuser [Befus et al. 2023]) all assume a continuous, constant decompression, which blurs the effect of acceleration in the shallow conduit and thus provides an average of the entire decompression path (Figure 1B). Although a continuously accelerating decompression path model would be the most comparable to advances in modeling BND and MND, it has yet to be developed. Instead, here we apply a recently developed two-stage decompression-diffusion model (two constant rates) by Hosseini et al. [2021] and Hosseini [2023], which attempts to better approximate continuously accelerating decompression. Although still limited, this approach allows users to resolve both an initial slow stage of decompression deeper in the conduit as well as a final faster stage just prior to fragmentation. By applying the two-stage model to diffusion-limited gradients in natural embayments, we find that this model generally provides better fits to the measured data, and total ascent time is increased by a minimum of 4–5× over existing models, largely driven by the slower initial stage [Hosseini et al. 2022].

Here, we apply both the simplified (constant rate) and updated (time-integrated) models for extracting decompression rates from bubbles, microlites, and melt embayments to a sample suite from the 1991 eruption of Mount Pinatubo, an event characterized by robust independent observations (e.g. plume height, precursory activity, eruption frequency). The 1991 eruption of Pinatubo is amongst the most closely observed and well-studied large-volume silicic eruptions in recorded history (see *Fire and Mud* [Newhall and Punongbayan 1996]). This allows us to address two important questions: 1) whether magma decompression rates derived from these three different petrologic techniques can be reconciled or integrated to create a more complete model of magma ascent from source to surface, and 2) through comparison with external observational and monitoring datasets, whether the petrologic record preserves evidence for what ended up being an escalation in eruptive energy.

2 THE 1991 ERUPTION OF MOUNT PINATUBO

Mount Pinatubo is located on the island of Luzon in the northwestern Philippines, along the Bataan arc and <200 km west of the Manila trench (Figure 2A). Over its 30,000-year eruptive history, Pinatubo has consistently produced large volumes of dacitic magma that preserve evidence of intrusion and mixing with hotter basalt [Newhall and Punongbayan 1996]. In the months leading up to the climactic eruption on June 15, 1991, there was significant volcanic unrest, including strong increases in seismicity, small ash emissions and, beginning on June 7, the extrusion of a hybrid andesitic lava dome [Pallister et al. 1996]. The andesitic lava extruded during this early dome formation has been shown to be the product of the injection and mixing of basalt into the dacitic magma reservoir [Pallister et al. 1996]. Between June 12–14, four larger erup-

tions produced vertical columns (19–24 km high), which increased in frequency with time and transitioned from dominantly hybrid andesite (59 wt.% SiO₂) to dacite (64 wt.% SiO₂) in whole-rock composition (Pallister et al. [1996]; Figure 2B). The andesitic scoria erupted during the June 12 vertical eruptions is identical to the dome andesite in terms of phenocryst assemblage and bulk composition but differs in vesicularity and groundmass crystallinity [Pallister et al. 1996].

Following these early vertical eruptions, a series of 13 surge deposits were produced during June 14–15 (Figure 2B). Although many of these eruptions were not witnessed directly, radar and infrared measurements indicate that plume heights ranged from 5–24 km. These surge-forming eruptions generally grew less intense with shorter repose intervals [Hoblitt 1996]. Hammer et al. [1999] analyzed MND of plagioclase in the degassed plug material that was erupted during these 13 surge-producing blasts, arguing that the pressure of the rising magma continuously increased over time, overcoming the confining pressure of a degassed plug at successively shorter time intervals. During this time, seismicity began to rapidly increase [Harlow et al. 1996] and culminated in the climactic eruption of June 15, beginning at 1:42 pm local time, which produced a Plinian column 34 km high and an umbrella cloud over 400 km in diameter that deposited ash predominantly to the southwest (Figure 2). The first major explosive eruption, occurring on June 12 at 8:51 am local time, is the focus of this study.

Extensive work has been done to understand the pre-eruptive conditions of the Pinatubo magma, which we use in this study as input parameters for decompression models. The dominant dacitic magma feeding the later explosive eruptions has a phenocryst assemblage of plagioclase and hornblende (with lesser amounts of cummingtonite overgrowths), Fe-Ti oxides, quartz, apatite, and anhydrite [Pallister et al. 1996]. The dacitic magma was stored at 7–11 km (220 ± 50 MPa) beneath Pinatubo based on Al-in-hornblende (rim) geobarometry, with magmatic temperatures around 780 °C based on Fe-Ti oxide geothermometry [Rutherford and Devine 1996]. Furthermore, the presence of cummingtonite rims on hornblende indicates a temperature of <800 °C and a pressure range of 200–320 MPa [Pallister et al. 1996], which agree well with the Al-in-hornblende geobarometry (220 ± 50 MPa). In addition to the mineral assemblage noted for the dacite, the hybrid andesite contains olivine, clinopyroxene, and biotite and yields an elevated Fe-Ti oxide temperature of 950 °C [Pallister et al. 1996]. Quartz- and plagioclase-hosted melt inclusions from the dacitic magma record pre-eruptive dissolved volatile contents of 5.5–6.4 wt.% H₂O, 55–78 ppm S, and less than 20 ppm CO₂ [Rutherford and Devine 1996].

Although several geospeedometry methods have been employed in previous studies to evaluate magma ascent for the 1991 eruptions of Pinatubo, none have yet examined the earliest Plinian eruptions. In addition, the two methods (BND and MND) were applied to samples from different parts of the eruption sequence, meaning we are unable to determine if and how they relate to one another. The BND-based decompression rate for the climactic June 15 eruption was previously determined by Toramaru [2006] to be 100 MPa s⁻¹, assuming

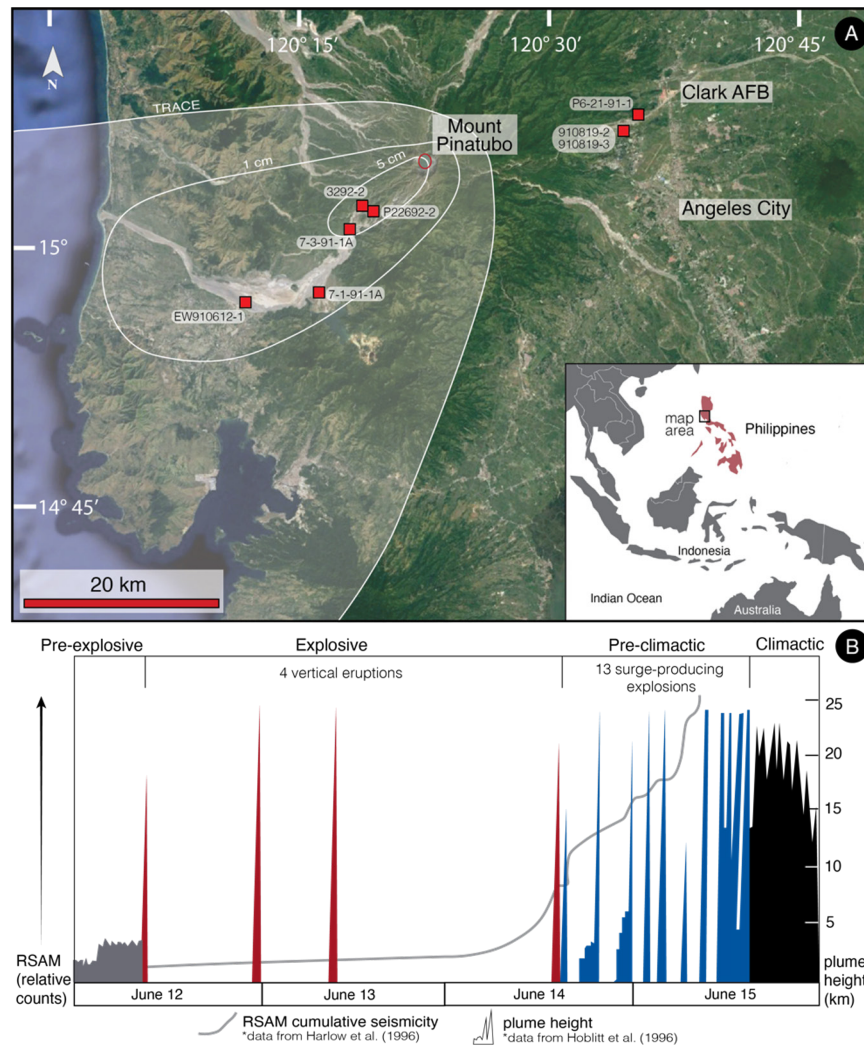


Figure 2: [A] Map of Mount Pinatubo and surrounding area, showing the site locations where samples were collected in 1991 and 1992. Inset shows the location of the map area. Isopach lines denote thickness of tephra deposits from the 8:51 am June 12 eruption [Paladio-Melosantos et al. 1996]. Samples within the isopach lines are from the 8:51 am June 12 eruption. Samples from the 10:51 pm June 12 eruption (910819-2 and 910819-3) and the climactic June 15 eruption (P6-21-91-1) were collected near Clark Air Force Base (AFB). The red circle marks the summit caldera that formed during the climactic eruption. [B] Generalized eruption timeline, as described in the main text. The explosive phase consisted of four vertical eruptions from June 12–14, with the pre-climactic phase characterized by 13 surge-producing explosions from June 14–15. Real-time Seismic Amplitude Measurements (RSAM) show that cumulative seismicity increased dramatically between June 14 and the onset of the climactic eruption on June 15 [Harlow et al. 1996].

homogeneous nucleation. By implementing models of heterogeneous nucleation, the calculated decompression rate is reduced to $\sim 4.5 \text{ MPa s}^{-1}$ [Shea 2017]; however, these rates are still several orders of magnitude faster than other geospeedometry results (i.e. microlites, embayments; $< 0.1 \text{ MPa s}^{-1}$ [Liu et al. 2007; Brugger and Hammer 2010]).

3 METHODS

3.1 Sample preparation

Eight pumice clasts and bulk ash material from the 8:51 am and 10:52 pm June 12 explosive eruptions, as well as three samples from the climactic 1:42 pm June 15 eruption, were obtained from the sample archives of the U.S. Geological Sur-

vey Cascades Volcano Observatory (Figure 2A). Seven of the eight samples from the 8:51 am eruption contained pumice clasts large enough to create thick sections for BND and MND analyses. These, and one pumice clast from June 15, were cut into billets, impregnated with epoxy using a vacuum system, and sent to National Petrographic Service for preparation of thick sections. Two of the climactic June 15 samples lacked pumice clasts large enough to create thick sections.

The remainders of each pumice sample, along with four samples of fine-grained material, were lightly crushed and sieved to obtain the 500–1000 μm size fraction. Quartz crystals containing embayments were then picked from this size fraction using a stereo microscope, where eleven glassy embayments were obtained from seven samples, five of which

have accompanying thick sections. Glassy embayments are quite rare in the Pinatubo products, where most embayments (~80 % of the examined crystal population) are either highly vesiculated or completely hollow. Glassy embayments analyzed in this work are derived from the June 12 eruptions, as only one glassy embayment was found in the June 15 samples. The embayments found in the June 15 samples were often vesiculated or crystallized and thus unsuitable for volatile measurements and diffusion modeling. Full sample information and analyses conducted on each sample are summarized in [Table 1](#).

3.2 Scanning electron microscopy (SEM)

All seven thick sections from the June 12 pre-climactic eruption, as well as one thick section from the climactic June 15 eruption, were analyzed for BND and MND. Thick sections were carbon-coated and images subsequently obtained at high vacuum using a Tescan TIMA SEM at the Montana Technological University Center for Advanced Material Processing. Operating conditions included an accelerating voltage of 15 kV, a working distance of 15 mm, and a beam current of 20 nA. Images were taken using a nested imaging scheme outlined in [Shea et al. \[2010\]](#) at magnifications of 250× (3 images), 500× (6 images), 1000× (12 images), and for MND, 2000× (12 images), providing a total of 33 images per thick section ([Figure 3](#)). When possible, areas with sheared or elongated bubbles were avoided as these areas make 3D (volumetric) projections difficult.

3.3 Image processing

SEM images were processed using Adobe Photoshop to produce tri-colored images (bubbles = black, glass = white, and crystals = gray) and to reconstruct thin or broken bubble walls ([Figure 3](#)). The processed images were then loaded into the FOAMS interface [[Shea et al. 2010](#)]. A minimum bubble size of 5 pixels was chosen (below this value, uncertainty exceeds 5 %), and samples were normalized to a known vesicularity of 0.53 associated with the June 12 scoria [[Pallister et al. 1996](#)]. The output vesicularity-corrected BND (N_{Vcorr}) is used to estimate the decompression rate using the calibration meter of [Toramaru \[2006\]](#), with two surface tension values (the energy required to nucleate and maintain a bubble; σ) explored: 0.06 N m⁻¹ for homogeneous nucleation and 0.025 N m⁻¹ for heterogeneous nucleation [[Shea 2017](#)].

We then compared these results with those obtained using the updated BND geospeedometer of [Hajimirza et al. \[2021\]](#). Input parameters for this model include mass discharge rate, initial pressure, temperature, crystallinity, wetting angle (θ), and conduit radius. We calculate an average mass discharge rate of 4.8–7.8 × 10⁶ kg s⁻¹ using an ejected volume of 4–6.5 million m³ dense rock equivalent for the 8:51 am June 12 eruption [[Paladio-Melosantos et al. 1996](#)] and by assuming a magma density of 2600 kg m⁻³, calculate a mass of 1.04–1.69 × 10¹⁰ kg of material erupted over a span of 38 minutes (based on seismic observation [[Wolfe and Hoblitt 1996](#)]). We iterate through different wetting angles between bubble and crystal surface (values of θ) and conduit radii until modeled BND values match the values determined from our SEM im-

ages. The wetting angle is dependent on the mineral phase and dictates whether heterogeneous or homogeneous nucleation occurs [[Hurwitz and Navon 1994](#)]. Homogeneous nucleation occurs if the contact angle θ is less than 60° (associated with plagioclase and pyroxene; correlated with higher surface tension values, $\sigma = 0.045$ – 0.083 N m⁻¹), and heterogeneous nucleation will occur when θ is greater than 90° (associated with hematite and magnetite; correlated with lower surface tension value, $\sigma = 0.017$ – 0.03 N m⁻¹) [[Hurwitz and Navon 1994](#)]. Complete model input parameters can be found in [Supplementary Material Table S1](#).

Processed images of the 2000× magnifications were then used for microlite textural analysis ([Figure 3D](#)). Images were analyzed using ImageJ to determine plagioclase microlite number density ($N_A = \#$ of crystals/mm²), crystallinity ($\phi_m = \text{microlite area/groundmass area}$), characteristic crystal size ($S_N = (\phi/N_A)^{1/2}$), and the volumetric number density ($MN_V = N_A/S_N$) for each pumice clast ([[Hammer and Rutherford 2002](#)]; [Table 2](#)). Plagioclase microlite crystallinity and microlite number density are determined on a bubble- and phenocryst-free (crystals > 50 μm) basis, where bubble volume was determined based on earlier FOAMS results. Twelve images were analyzed per clast for five clasts from the 8:51 am June 12 eruption; the other three thick-sectioned samples, including one from the June 15 eruption, were completely glassy and thus unable to be analyzed for MND. We characterize only plagioclase microlites, the most abundant groundmass mineral phase, and only consider crystals <50 μm in length as microlites, following [Benage et al. \[2021\]](#). Other crystal phases (i.e. oxides) and plagioclase microlites larger than 50 μm are not included in the microlite calculations.

To determine the decompression conditions that lead to observed MN_V and ϕ values for the June 12 eruption, we applied the decompression model SNGPlag developed by [Andrews and Befus \[2020\]](#). SNGPlag utilizes a range of plagioclase microlite growth and nucleation rates and allows for the simulation of single-step, multi-step, accelerating, and continuous decompression pathways. In the SNGPlag model, the nucleation and growth rates at every time step are updated based on the calculated degree of supersaturation, based on the difference between the model-calculated crystallinity and the equilibrium crystallinity (calculated using MELTS [[Gualda et al. 2012](#)]). The supersaturation was then used to calculate the instantaneous plagioclase nucleation and growth rates for the given pressure and temperature conditions. We included the presence of plagioclase phenocrysts (an instantaneous volume fraction at each timestep is calculated by MELTS [[Gualda et al. 2012](#); [Ghiorso and Gualda 2015](#)]) in all model simulations. In all of our modeling, we used microlite growth and nucleation rates based on the experimental calibration of [Befus and Andrews \[2018\]](#). We ran models using constant decompression rates ranging from 0.1–100 MPa hr⁻¹ (0.001–1 m s⁻¹), as well as simulating a 10× accelerating and single-step decompression path. Complete model input parameters can be found in [Supplementary Material Table S2](#).

Table 1: List of samples studied, indicating location, eruption, and which analyses were performed for each sample. ×'s denote samples that had pumice clasts suitable for MND and/or BND analysis.

Sample #	Location	Description	Eruption	Microlites	Bubbles	Embayments
7-1-91-1A	Mt. Bagang	6/12/91 tephra (scoria)	12th	×	×	3
EW910612-1	Castillejos	6/12/91 tephra	12th			1
P22692-2A	SW flank	6/12 scoria	12th		×	
P22692-2C	SW flank	6/12/91 tephra	12th	×	×	
P22692-2E	SW flank	Upper 1 cm tephra bed	12th	×	×	3
3292-2A	SW flank	6/12 tephra, scoria and dacite pumice	12th	×	×	1
3292-2C	SW flank	Blast above 6/12 tephra	12th		×	1
7-3-91-1A	DMA Mt.	Lowermost unit Pinatubo tephra	12th	×	×	1
910819-2	Clark AFB [†]	6/15/91 tephra, top-Plinian fall	15th			
910819-3	Clark AFB	6/15/91 tephra, mid-Plinian fall	15th			1
P6-21-91-1	Clark AFB	Pinatubo tephra	15th		×	

[†] Clark Air Force Base

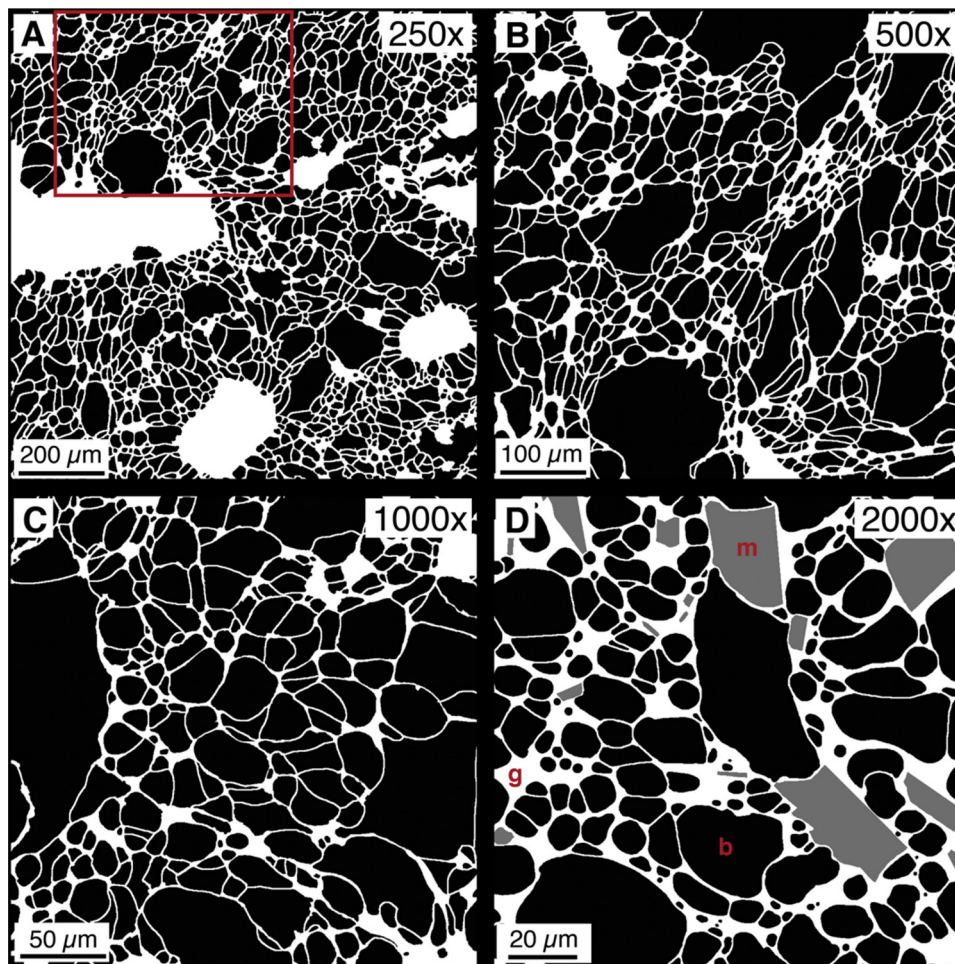


Figure 3: SEM photomicrographs were collected using a nested imaging scheme, described by Shea et al. [2010]. Images taken at 250× [A], 500× [B], 1000× [C], and 2000× [D] magnifications were processed in Adobe Photoshop to reconstruct bubble walls and to create tri-colored images, where black = bubble (b), white = glass (g), and gray = microlite (m) (2000x images only). The red box in [A] outlines part of the nested image in [B].

3.4 FTIR analysis of volatile concentrations

Glassy embayments were mounted on round slides in Crysalbond and double-polished to produce crystal wafers that

intersect the length of the embayment on both sides. Embayments measured 50–180 μm in length and every embayment had a bubble present at the mouth. Transect measurements of volatile concentrations were conducted using a Nico-

let iN10 MX infrared microscope and integrated spectrometer at Montana State University. Transects were measured along the length of the embayment using a liquid-nitrogen-cooled MCT-A detector with an aperture of $20 \times 20 \mu\text{m}$, a step size of $10 \mu\text{m}$, a spectral resolution of 8 cm^{-1} , and 256 scans per spot. The CO_2 peak, measured at a wavelength of 2350 cm^{-1} , was absent; the H_2O absorbance was measured using the total H_2O peak (3570 cm^{-1}) and was converted to concentration using a linear baseline and the Beer-Lambert law:

$$C = \frac{A \cdot M}{\rho \cdot \epsilon \cdot t} \quad (1)$$

where C is the concentration (wt.%), A is the measured absorbance (peak height), M is the molecular mass of the volatile species (g mol^{-1}), ρ is the density of the glass (g L^{-1}), ϵ is the molar absorption coefficient ($\text{L mol}^{-1} \text{ cm}^{-1}$), and t is the wafer thickness (cm), determined using both a digital micrometer and the reflectance fringe method of Wycoczanski and Tani [2006]. The micrometer and reflectance methods were generally in agreement; however, if they differed by $>4 \mu\text{m}$, only the reflectance-based thickness was used. To convert from measured absorbance values to H_2O concentration, we assume initial values of 2600 kg m^{-3} for ρ and $80 \text{ L mol}^{-1} \text{ cm}^{-1}$ for ϵ (based on a rhyolitic glass composition) and then iterate through the Beer-Lambert calculation until values converge, as both parameters are H_2O -dependent [Skirius et al. 1990; Leschik et al. 2004]. The error on H_2O measurements ranges from ± 0.05 to 0.44 wt.%, with an average of ± 0.22 wt.%. Full transect data can be found in Supplementary Material Table S3.

3.5 Electron probe micro analysis (EPMA)

Due to the changing whole rock composition of erupted materials over the course of the pre-climactic eruptions, compositional analyses of the embayment glasses are necessary to confirm the validity of multiple diffusion model parameters, including the temperature, density, and diffusion coefficients, which all depend on the major elemental composition. Crystal wafers were placed in 1-inch epoxy mounts, carbon-coated, and analyzed for major and volatile elements (Si, Al, Ti, Na, K, Mg, Ca, Fe, Mn, Cl, S) using a Cameca SX-100 electron microprobe at Oregon State University. Transects were analyzed along the length of the embayment using a $10\text{-}\mu\text{m}$ defocused beam and a step size ranging from 15 to $22 \mu\text{m}$. Operating conditions included an accelerating voltage of 15 keV and a beam current of 10 nA . Major elements had counting times that ranged from $10\text{--}30$ seconds where analytical errors were calculated based on analyses of the silicate glass standard (Smithsonian Microbeam Standard VG 568). Sulfur had a longer counting time of 90 seconds, resulting in a detection limit of ~ 100 ppm. Totals were calculated by adding in the known melt H_2O concentration (determined from FTIR analysis of the interior part of the embayment), and all other elements were normalized using a mean atomic number correction. Analyses with totals below 98.5% or above 101.5% were discarded. Full major element transect data can be found in Supplementary Material Table S4.

3.6 Diffusion modeling

Diffusion modeling was conducted using a constant-rate decompression model presented in Myers et al. [2018], adapted from Liu et al. [2007]. A range of decompression rates and fragmentation pressures (where diffusion ceases due to rapid glass quenching) were iterated through to determine the rate that best fit the measured volatile gradients. The H_2O and CO_2 conditions at the melt-bubble boundary are determined by solubility relationships at a given pressure and updated at every decompression step [Liu et al. 2005]. With these boundary conditions, we assume equilibrium between the gas bubble present at the mouth of the embayment and the surrounding magma. The best-fit model was determined by identifying the decompression rate and fragmentation pressure that produced the lowest misfit value, determined by a Chi-squared test of the difference between the measured and modeled gradients. Due to the lack of CO_2 measured in the melt, all models were run assuming open-system degassing. Best-fit model results can be found in Supplementary Material Table S5. The constant-rate code and all relevant documentation are available on GitHub and archived on Zenodo*.

To better approximate the effect of accelerating decompression on resulting volatile gradients, we also employed a two-stage decompression-diffusion code [Hosseini et al. 2022; Hosseini 2023]. This model allows for an accelerating pathway to be constrained by two separate constant decompression rates (Figure 1). The two-stage decompression code first simulates volatile diffusion during constant-rate decompression from the initial storage pressure to some intermediate pressure (the pressure at which the ascent rate changes). Once the model reaches the intermediate pressure, the current $\text{H}_2\text{O} \pm \text{CO}_2$ concentration gradient is then used as the initial condition for the second stage of decompression. The second stage consists of another constant decompression rate, and diffusion occurs until the system reaches the fragmentation depth. These three parameters, both the first- and second-stage decompression rates and the intermediate pressure, are cycled through as free variables, and collectively are used to determine the best fit conditions to the measured profile. A major challenge with the application of the two-stage model is a lack of constraints on the initial, slow stage of decompression, mostly in H_2O -only systems, which can trade-off with intermediate pressure to permit similarly good fits to the measured profiles with vastly different initial timescales [e.g. Lloyd et al. 2014]. Although we recognize this limitation and thus caution that, in H_2O -only systems, the two-stage model results should be interpreted in the context of other independent observations when possible, we nevertheless believe a two-stage approach better reproduces the degassing and diffusion dynamics of natural systems. Additionally, owing to the non-uniqueness of solutions to the initial stage of decompression, the uncertainty on the presented rates assumes the model recovers the true transition pressure. In applying this model to Pinatubo embayments, we assume that initial decompression was slow enough for the embayment interior to re-equilibrate, such that the transition pressure should be within ± 20 MPa of

*<https://zenodo.org/record/7803186>

the interior saturation pressure. This allows us to constrain the range of transition pressures cycled through in the model. The two-stage code and all relevant documentation are available on GitHub and archived on Zenodo*.

4 RESULTS

4.1 Electron probe micro analysis

The calibrations and assumptions inherent in the following decompression models first require an understanding of the embayment glass composition. Although the June 12 eruptions produced a hybrid andesite (whole rock composition), the composition of the embayment glass in all June 12 quartz hosts is rhyolitic, with an average of 75.2 wt.% SiO₂ (Supplementary Material Table S4). This allows us to use rhyolitic diffusion coefficients and solubility relationships [Liu et al. 2005; Zhang et al. 2007], densities (2350 kg m⁻³ [White and Harris 1997]), and the temperature (780 °C [Rutherford and Devine 1996]) associated with the dacite magma in all models. Measured major element concentrations are consistent within error along the length of the embayment, and both Mn and S fall below the detection limits (800 and 100 ppm, respectively) (Supplementary Material Table S4).

4.2 Bubble number density

The corrected volumetric number density ($N_{V,corr}$) for the seven clasts representing the first June 12 event ranged from 2.3×10^5 – 4.2×10^6 mm⁻³ (average = 1.6×10^6 mm⁻³). The $N_{V,corr}$ of the single clast from the climactic June 15 eruption falls within the range of the pre-climactic samples, with an $N_{V,corr}$ of 2.01×10^6 mm⁻³. Polacci et al. [2001] found similar values for the climactic dacite pumice, with $N_V = 3.0$ – 9.0×10^6 mm⁻³. These values were then used to extract a decompression rate, first using the approach of Toramaru [2006] and then applying the recent calibration from Hajimirza et al. [2021]. Initial magma is assumed to be stored at 220 MPa, 780 °C, and to contain a phenocryst crystallinity of 38 % [Pallister et al. 1996]. If we assume homogeneous nucleation ($\sigma = 0.06$) and apply the Toramaru [2006] calibration, observed BNDs for all samples correlate to decompression rates ranging from 14.5–100 MPa s⁻¹ (Figure 4). If instead we assume heterogeneous nucleation ($\sigma = 0.025$), the corresponding decompression rates are nearly an order of magnitude lower, ranging from 2.5–17 MPa s⁻¹.

Through applying the Hajimirza et al. [2021] BND ascent rate meter to our samples, where temperature, crystallinity, and nucleation contact angle (θ) are kept constant, the observed BND measurements are best fit by decompression rates ranging from 0.09–0.87 MPa s⁻¹ (average = 0.39 MPa s⁻¹), with a θ of 155° (heterogeneous nucleation), and a conduit radius of 14–23 m (Figure 4). This fits well with the observed conduit diameter for the June 12 events (10s of meters [Gerlach et al. 1996]). There is no discernable difference in converted ascent rates between the June 12 and June 15 samples; however, based on early assessment, the June 15 BND measurements require a larger conduit radius (80–130 m [Hajimirza et al. 2021]).

* <https://zenodo.org/record/10042159>

4.3 Plagioclase microlite textural data

For the five thin sections from the June 12 tephra, microlite number density (MN_V) ranges from 4.2 – 8.4×10^4 mm⁻³ and microlite crystallinity (ϕ) is between 0.06–0.09 (Table 2). In comparison, many of the June 14–15 pre-climactic surge deposits made up mostly of dense degassed plug material have higher values, with maximum MN_V values between 7.1×10^7 – 3.1×10^9 mm⁻³ and ϕ of 0.01–0.22 [Hammer et al. 1999]. However, microlites from the June 12 deposits have a larger characteristic crystal size (S_N), ranging from 10–12 μ m, than that found for the surge-forming deposits, which range from 0.49–1.80 μ m [Hammer et al. 1999]. Some highly vesicular samples from the surge-producing deposits studied by Hammer et al. [1999], as well as the climactic sample and two of the June 12 samples analyzed here, were found to lack microlites altogether. Based on the interpretations from Hammer et al. [1999], we assume that the three microlite-free June 12 samples are produced by ascent timescales totaling less than 40 minutes or decompression rates ≥ 0.08 MPa s⁻¹.

Table 2: Microlite crystallinity, characteristic size (S_N), and number density (MN_V) calculation results.

Sample	# of microlites	ϕ	S_N (μ m)	MN_V (mm ⁻³)
7-1-91-1A	53	0.092	11.3	6.3×10^4
7-3-91-1A	43	0.067	11.0	5.1×10^4
P22692-2C	60	0.080	12.4	4.2×10^4
P22692-2E	63	0.060	11.1	4.4×10^4
3292-2A	74	0.093	10.3	8.4×10^4

Calculated volumetric microlite volume densities (MN_V) are recreated in SNGP_{lag} using the Befus and Andrews [2018] nucleation and growth rates. When assuming a single-step decompression pathway, similar to what Hammer et al. [1999] used to model the surge deposits, our observed MN_V were reproduced using decompression rates of 39–92 MPa hr⁻¹ (0.011–0.025 MPa s⁻¹), although two samples were unable to be fit with a single-step decompression. Assuming a constant rate decompression path, good fits to the observed data were produced with rates of 11–43 MPa hr⁻¹ (0.003–0.012 MPa s⁻¹) (Figure 5). These rates agree well with those determined for the June 14–15 surge-forming eruptions, where Befus and Andrews [2018] remodel microlite data from Hammer et al. [1999] under constant decompression and find best fit rates ranging from 5–50 MPa hr⁻¹ (0.0014–0.014 MPa s⁻¹). Finally, when we assume a decompression path that accelerates by an order of magnitude from start to end, we find that our observed data are fit by average rates of 7–26 MPa hr⁻¹ (0.002–0.007 MPa s⁻¹) (Figure 5).

Earlier work by Befus and Andrews [2018] find that some surge deposit samples are unable to be fit by the continuous decompression models and may instead be recording unsteady decompression, as suggested by Hammer et al. [1999], whose single-step modelling required stalling to reproduce observed crystallinities in the June 14–15 surge forming eruptions [Hammer et al. 1999]. Intriguingly, for our June 12 data,

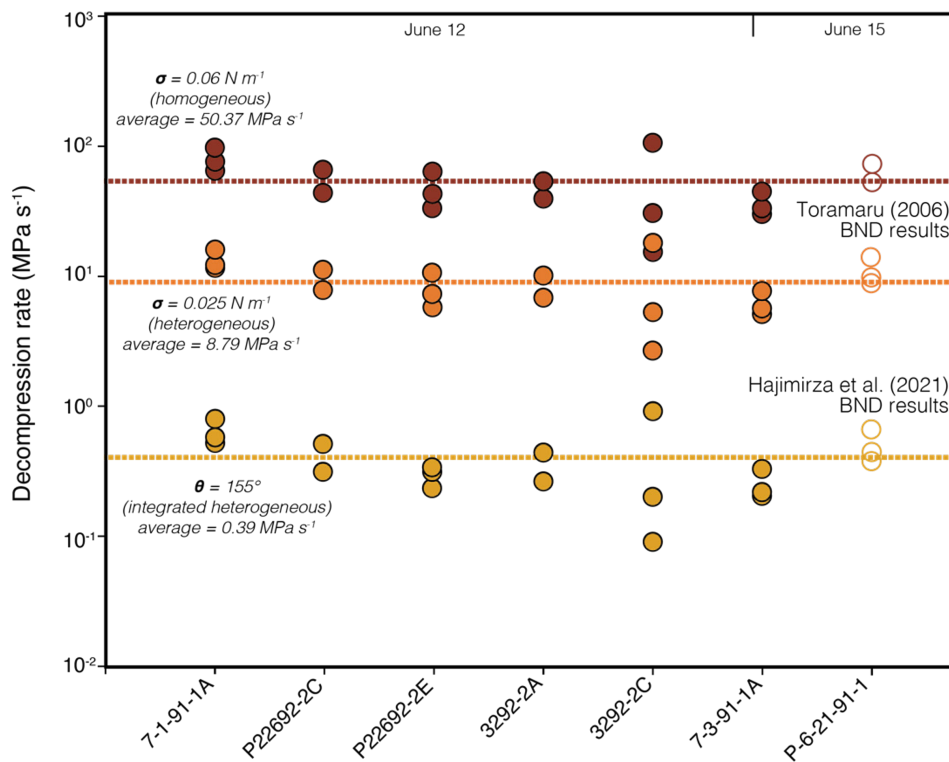


Figure 4: Decompression modeling results for individual pumice clasts based on bubble number density, using the model by Toramaru [2006] and the time-integrated model by Hajimirza et al. [2021]. Surface tension values of 0.06 and 0.025 N m⁻¹ were chosen for the Toramaru [2006] models to represent homogeneous (dark gray circles) and heterogeneous (medium gray circles) nucleation, respectively. Non-integrated, homogeneous models (dark gray circles) result in the highest calculated decompression rates, while integrated, heterogeneous models from Hajimirza et al. [2021] (light gray circles) result in slower calculated decompression rates. Open symbols represent the climactic June 15 sample. Dotted horizontal lines represent the average decompression rate for each of the three BND modeling approaches.

models that included even a short stalling event at 70 MPa produced crystallinities that were up to an order of magnitude greater than what was observed in the natural samples.

4.4 Volatile diffusion in embayments

We find that the interiors of the June 12 embayments contain 1.82–4.32 wt.% H₂O and lack detectable CO₂ (<20 ppm) and S (<100 ppm). Embayment rims have lower H₂O concentrations ranging from 1.05–2.46 wt.%, and again lack measurable CO₂ and S (see Figure 6 for one example embayment profile). Interior embayment H₂O contents represent saturation pressures of 26–113 MPa, with an average of 60 MPa [Newman and Lowenstern 2002]. In comparison, melt inclusions from the June 14–15 phase of the eruption preserve volatile contents of 5.5–6.4 wt.% H₂O, less than 20 ppm CO₂, and 55–77 ppm S [Rutherford and Devine 1996], placing them at saturation pressures of 170–220 MPa [Rutherford and Devine 1996]. This provides us with two possible starting conditions for our diffusion modeling: the inferred magma storage pressure of 220 MPa or the embayment interior saturation pressures of 26–113 MPa, which would be akin to stalling or slow ascent within the conduit. Based upon the modeling results from microlites, we prefer the melt inclusion start, as it represents

ascent through the entire conduit, but we explore both options below.

Using the magma storage pressure of 220 MPa and a H₂O concentration of 6.35 wt.% as the initial model conditions, we find that six of 11 embayments are modeled successfully using a constant-rate decompression model with no stalling or acceleration. Extracted decompression rates range from 0.003–0.095 MPa s⁻¹ (average = 0.032 MPa s⁻¹) (Figure 7), equivalent to ascent rates of 0.12–3.72 m s⁻¹ (average = 1.24 m s⁻¹) when assuming a lithospheric density of 2600 kg m⁻³, with best-fit fragmentation pressures generally ranging from 1–40 MPa. If we instead use the H₂O content of the embayment interior and the corresponding pressures as the decompression model starting conditions, eight of 11 embayments are fit with the constant-rate diffusion model. Best-fit decompression rates for this starting condition produce a higher range from 0.043–0.48 MPa s⁻¹ (average = 0.174 MPa s⁻¹) (Figure 7). These decompression rates are equivalent to ascent rates of 1.69–18.82 m s⁻¹ (average = 6.82 m s⁻¹).

As previously discussed, a continuous, constant-rate decompression path is likely not representative of natural magma, as ascent velocity should increase toward the surface due to H₂O exsolution and an increase in magma buoyancy [Burgisser and Degruyter 2015]. Additionally, although the use of the embay-

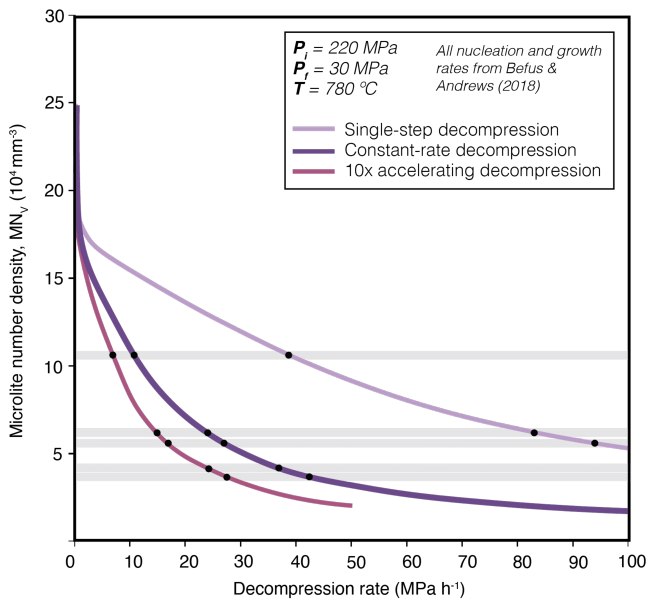


Figure 5: Microlite number density values resulting from SNGPLag decompression modeling using single-step (light purple curve), constant-rate (dark purple curve), and 10 \times accelerating (pink curve) decompression paths, all modeled using the nucleation and growth rates from Befus and Andrews [2018]. Observed microlite number densities for the June 12 pumices are shown by the five horizontal gray bars. Inset box shows input parameters used for all model runs, including a starting pressure of 220 MPa, a fragmentation pressure of 30 MPa, and a temperature of 780 $^{\circ}\text{C}$.

ment interior as starting conditions to model measured profiles leads to a larger number of good fits, experiments have shown that this approach can produce decompression rates that are $\sim 2\text{--}5\times$ faster than experienced by the embayment [Hosseini et al. 2023]. Therefore, we applied a newly developed two-stage decompression-diffusion model to the same suite of embayments above. We again use the melt inclusion starting conditions (initial pressure = 220 MPa, initial H_2O = 6.35 wt.%). The fragmentation pressure was based on the pressure associated with the H_2O content at the embayment mouth, which ranges from 0–68 MPa.

We find that the two-stage model provides good fits for the greatest number of embayments ($n = 9$ of 11), where the remaining two embayments were unable to be fit by any model. These two embayments had abnormally shaped profiles, with lower H_2O contents in the interior and at the rim and higher concentrations in the middle, potentially due to interference with the host crystal (i.e. embayment not fully intersected) or variation in sample thickness along the measured transect. All best-fit two-stage decompression models require the presence of an initially slow ascent phase (average $dP/dt = 0.008 \text{ MPa s}^{-1} = 0.29 \text{ m s}^{-1}$), followed by a much faster period of ascent near the surface (average $dP/dt = 0.273 \text{ MPa s}^{-1} = 10.72 \text{ m s}^{-1}$) (Figure 7).

Importantly, as observed by the two previous methods, there are good fits found to the modelled embayment data with all three sets of modeling parameters explored, however

the resulting timescales are orders of magnitude apart (e.g. Figure 6). For instance, depending on the starting conditions (H_2O content) and code framework (constant decompression vs. multi-stage) decompression times for one embayment shift from 4 minutes to 22 hours (Figure 6). Although one model might intuitively feel more accurate, it is challenging to resolve which is truly the path experienced if all model parameters can be used to produce a good fit.

5 DISCUSSION

5.1 Accounting for non-linear decompression

When using the linear, continuous decompression models for extracting ascent rate, we find that estimates for the June 12 Pinatubo eruption vary by up to three orders of magnitude between microlite number density, embayment volatile diffusion, and bubble number density (0.005 to $>10 \text{ MPa s}^{-1}$; Figure 8), with little agreement between each individual tool. This offset has been previously observed (compiled by Shea [2017]); however, this study presents the first dataset demonstrating that for a single pumice sample, the disagreement still holds. It could be that this difference is due to the kinetic limitations of each technique such that each will be weighted toward different regions of the conduit system [e.g. Benage et al. 2021; Myers et al. 2021] or that the rates retrieved are limited by the modeling parameters that have been used to extract decompression information.

By applying three newly updated decompression models, which consider the nonlinearity of magma ascent to differing degrees, we find that the range of decompression rates extracted collapses by about an order of magnitude (Figure 8). In addition, we find that the geospeedometry results are in better agreement with each other, where the decompression rates retrieved from the first stage of the embayment diffusion model (average = 0.008 MPa s^{-1}) align closely with the average decompression rate obtained via MND modeling (0.005 MPa s^{-1}), and the decompression rates from the second stage of the embayment diffusion model (0.273 MPa s^{-1}) now align well with those obtained from BND models ($0.085\text{--}0.87 \text{ MPa s}^{-1}$). Much of the collapse in decompression rates obtained from the three methods is from the almost two orders of magnitude decrease observed in BND. Arguably, these results imply that the two-stage embayment diffusion model is capable of resolving information retrieved from the combination of both the BND and MND methods.

There is still some degree of offset between rates recovered from BND and MND (recorded as a two order of magnitude increase in embayment decompression rate), although all techniques now implement time-integrated ascent pathways. This supports earlier interpretations that this offset is likely due to the inherently different kinetic processes controlling the nucleation and growth of bubbles and microlites. For example, when measuring the Pinatubo surge forming deposits, Hammer et al. [1999] show that there is a ~ 40 -minute nucleation lag ($\sim 0.1 \text{ MPa s}^{-1}$) where ascent rates exceeding this will not produce any microlites, which skews crystallinity-based applicability to slower ascent timescales. Likewise, heterogeneous nucleation of bubbles may require up to 50 MPa of decompression

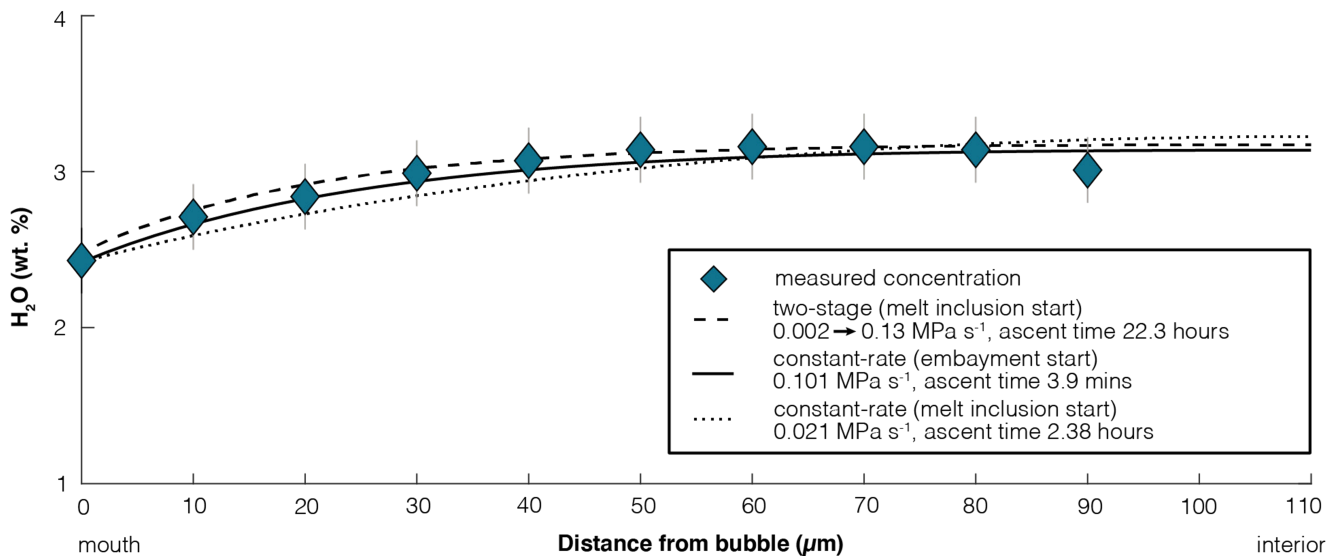


Figure 6: Measured H₂O profile from a single embayment (3292-2C-1) shown as teal diamonds, with three modeled scenarios shown. These three modeling scenarios simulate constant decompression from a melt inclusion storage pressure to quench (black dotted line), constant decompression from the pressure associated with the interior of the embayment (black solid line), and two-stage decompression from the melt inclusion storage pressure (black dashed line). While these three modeling scenarios can similarly reproduce the measured profile, the resulting total ascent timescales between the constant rate and two-stage approaches vary by 10s of hours.

sion to reach the necessary supersaturation levels [Shea 2017], skewing results toward the shallower conduit, often characterized by faster decompression.

Ultimately, this dataset suggests that the two-stage embayment method may be the most comprehensive method for determining ascent-driven magma decompression rates both at depth and near the surface. The biggest limitation is that embayments may not be found in every eruption or, when present, may be marred by textures that preclude their use in diffusion-based studies [e.g. Ruefer et al. 2021]. In this case, we suggest that using bubble number density and microlite crystallinity in tandem may provide similar decompression pathway resolution through the conduit system.

5.2 Comparison with other decompression rate estimates

Previous studies have focused on the topic of magma ascent rates for different portions of the Pinatubo eruption sequence. For instance, the BND speedometer developed by Toramaru [2006] has been used to calculate decompression rates of up to 100 MPa s⁻¹ for the climactic June 15 eruption. This calculation, however, assumes homogenous nucleation. Shea [2017] argues that heterogeneous nucleation is more feasible for most systems, potentially facilitated by nanolites of magnetite, resulting in a decompression rate of 4.6 MPa s⁻¹ for the climactic June 15 event. These values, however, are still several orders of magnitude greater than the BND modeling results for the June 15 event presented by Hajimirza et al. [2021] (0.06–0.62 MPa s⁻¹) when modeling time-integrated heterogeneous nucleation on magnetite crystals. These extreme variations in results from a single geospeedometer emphasize the influence of input parameters, in this case surface tension, and model calibration on extracted decompression rates. This is

an important limitation of decompression modeling, as also observed in our embayment modeling (Figure 6, Figure 7) and in the CSD modeling (Figure 5).

Hammer et al. [1999] examined dense tephra produced during the June 14–15 pre-climactic eruptions. Based on MND and volatile content, they concluded that magma that produced the dense tephra rapidly ascended from depth to shallow pressures of 6–16 MPa, where it stalled for 28–262 minutes (~4.4 hours). This step-function decompression path results in an initial stage of high nucleation (from ~40–170 minutes), followed by a period of crystal growth (after ~170 minutes) to reproduce observed textures. However, using experiments simulating time-integrated nucleation and growth of plagioclase microlites, Befus and Andrews [2018] re-model the MND measurements from Hammer et al. [1999] and determine that constant decompression rates of 0.001–0.005 MPa s⁻¹ could reproduce observed values. The rates presented by Befus and Andrews [2018] are comparable to those we derived for the June 12 samples using the same SNGP_{lag} model and decompression pathway, further highlighting the importance of the experimental calibration on extracted rates.

Despite the observed increases in plume height and seismic energy release leading up to the climactic eruption [Harlow et al. 1996; Hoblitt 1996], the collective decompression rates obtained from the two petrologic speedometers able to be assessed throughout the eruption sequence (BND and MND) do not show any evidence of systematic changes over time (Figure 9). This suggests that the observed increases in eruptive intensity were not primarily controlled by the magma ascent rate. Cassidy et al. [2018] suggest four scenarios for explosive eruption controls based on degassing style and viscos-

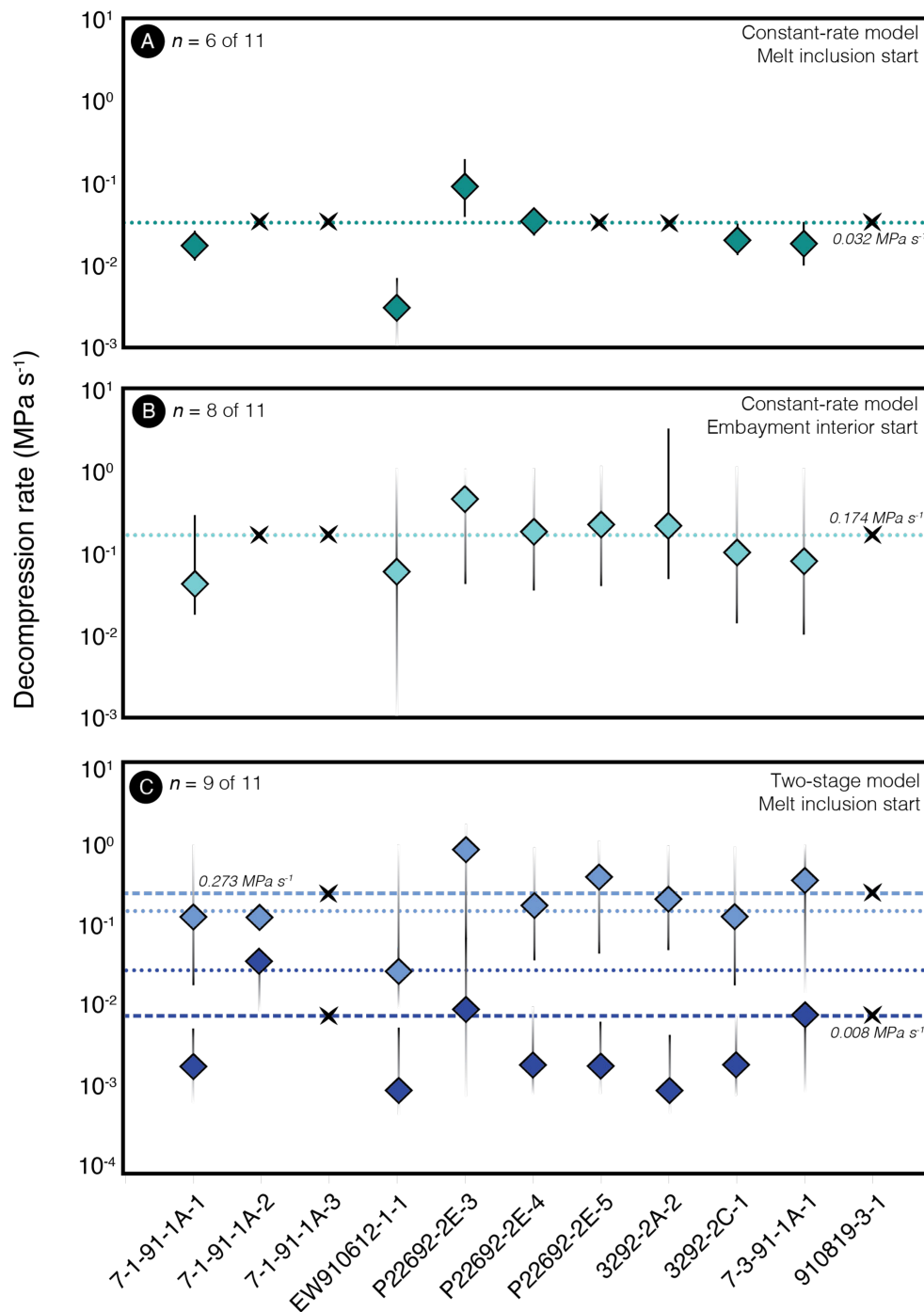


Figure 7: Results for embayment diffusion modeling. [A] Continuous, constant decompression-diffusion modeling using the melt inclusion starting condition results in good fits for six of 11 embayments, with an average decompression rate of 0.032 MPa s^{-1} (dark blue dotted line). [B] Constant-rate modeling using the embayment interior saturation pressure as the starting pressure results in good fits for eight of 11 embayments, with an average decompression rate of 0.174 MPa s^{-1} (light blue dotted line). [C] Implementing a two-stage model results in good fits for nine of 11 embayments, with the first stage of decompression being slower than the melt inclusion average (dark blue dashed line; 0.008 MPa s^{-1}) and the second stage being slightly faster than the embayment interior average (light blue dashed line; 0.273 MPa s^{-1}). Two embayments were unable to be successfully modeled using any of the three modeling approaches. Sample that were not successfully modeled (i.e. misfit > 1) are indicated with black X's. When the range in decompression rates producing a good model fit was within the search grid of values, the error is indicated by a solid, truncating black line. The fading error bars represent model runs where the range in decompression rate was not constrained within the values iterated through.

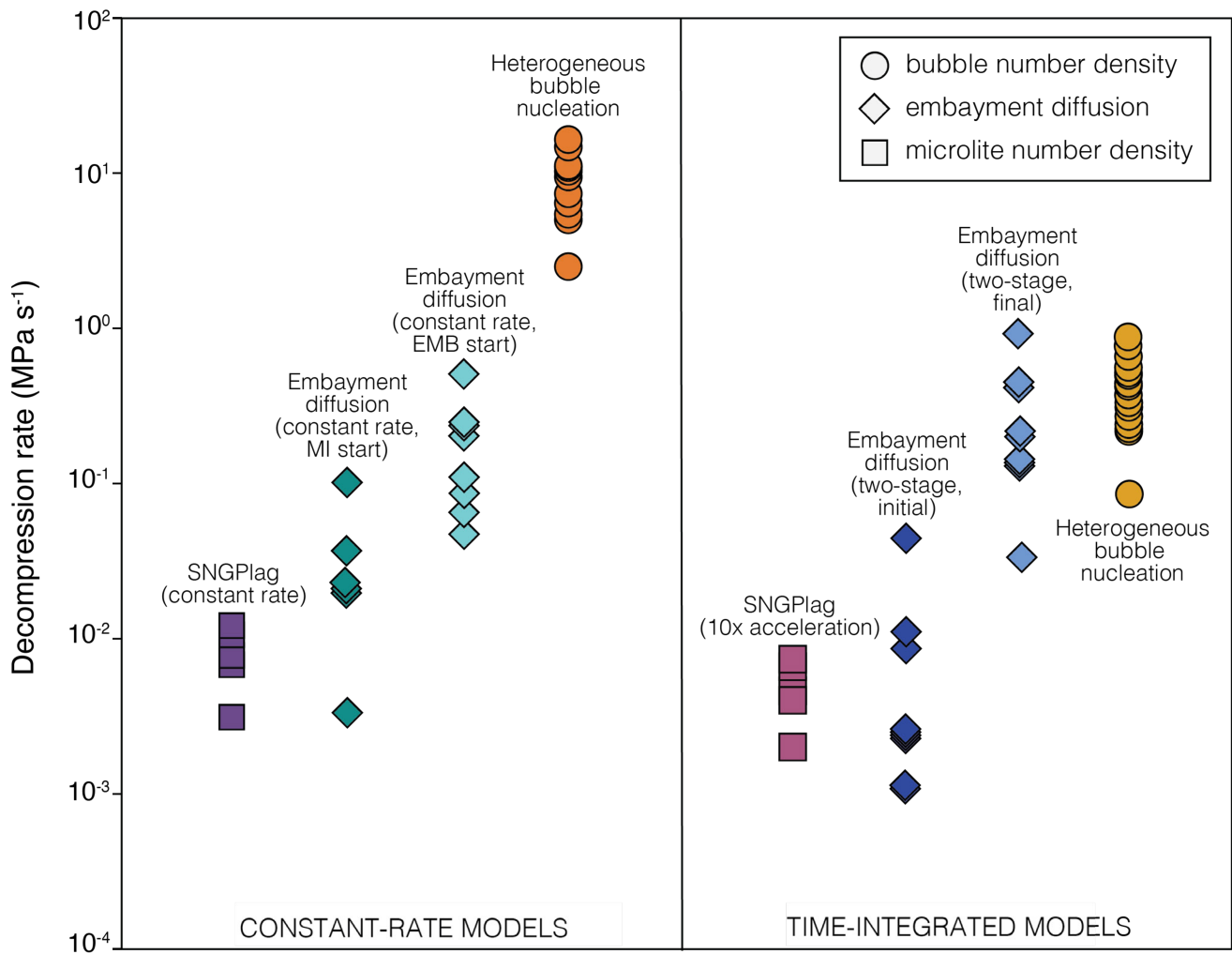


Figure 8: Comparison of decompression rate results using traditional (constant-rate) models (left) and updated (time-integrated) models (right). When using the traditional models, we find a 3–4 order of magnitude spread across the dataset. By implementing the updated models, we find better agreement between the speedometers, where the initial stage of decompression from the embayment model (dark blue diamonds) overlaps well with the SNGPlag model (pink squares) and, most notably, the second stage of decompression from the embayment model (light blue diamonds) correlates well with the updated model of [Hajimirza et al. \[2021\]](#) simulating heterogeneous bubble nucleation (light gray circles).

ity: ascent-controlled, exsolved gas/plug controlled, viscosity-controlled, or decompression-wave controlled. In the following section we argue that rather than a “bottom-up” ascent control, the intensity of the pre-climactic Pinatubo eruptions was instead controlled by the confining pressure of a shallow plug, as was suggested by [Hoblitt \[1996\]](#) for the June 13–14 eruptions, or by an “unzipping” enlargement of the caldera vent.

5.3 Top-down control of magma ascent

One interesting result from the combined petrologic tools, as recorded independently by the two-stage embayment model, is that for the June 12 eruption there appears to be an initial slower stage of decompression followed by a shorter, faster final ascent, where the total time of ascent from the embayment model ranges from two hours up to two days. This ascent time is dominated by the first, slower stage. The recognition

of a dominant slower initial stage of decompression was also a primary result of the development and application of the two-stage model to previously studied silicic caldera-forming eruptions [[Myers et al. 2018](#); [Hosseini et al. 2021](#)]. Confidence for the legitimacy for this initial slow phase can when the method was applied to embayments from the 1980 eruption of Mount St. Helens. It was found that the best fit ascent time associated with the initial slower phase ($0.008\text{--}0.01\text{ MPa s}^{-1}$) aligns closely with visual estimates for the timing between the initial lateral blast and subsequent Plinian explosion 3.5 hours later [[Scandone and Malone 1985](#); [Eichelberger 1995](#); [Hosseini et al. 2022](#)]. For Pinatubo, the timing of this initial slow stage of magma ascent (hours to two days) coincides with the later emplacement of an andesitic lava dome as observed at the surface, where growth was intermittent between June 7–12 [[Hoblitt 1996](#)]. The overlap in timescale between these two observations suggests a link in the process, whereby the

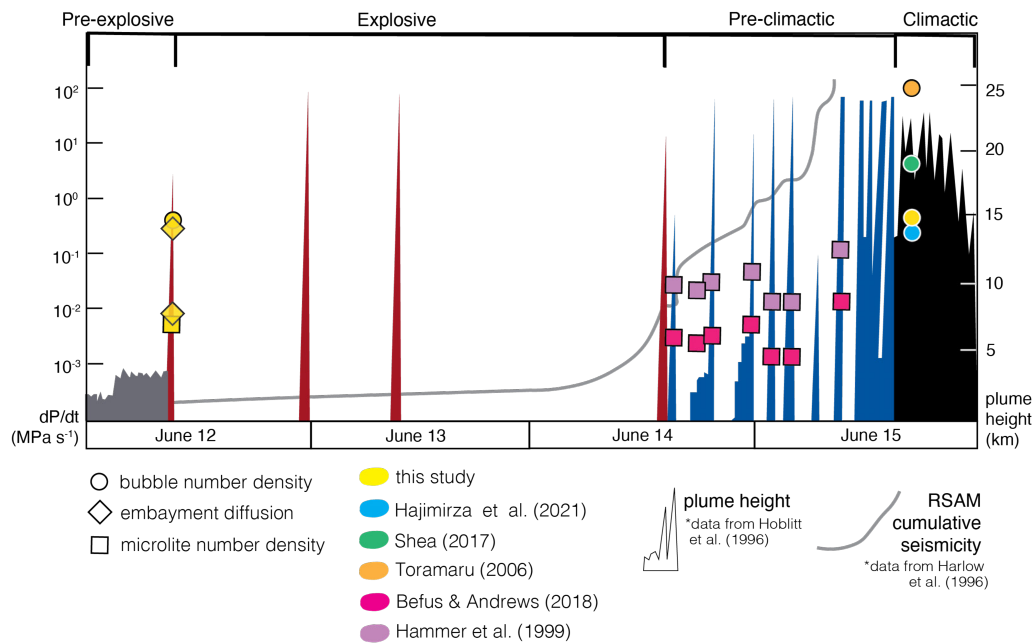


Figure 9: Compilation of observational (plume height) and seismic (Real-time Seismic Amplitude Measurement; RSAM) data from June 12–15 [Harlow et al. 1996; Hoblitt 1996] with superimposed average decompression rates determined by microlite number density [Befus and Andrews 2018, this study], bubble number density [Hajimirza et al. 2021, this study] and embayment diffusion modeling (this study). Plume height colors correlate with eruptive phase: gray = pre-explosive eruptions, red = explosive vertical eruptions, blue = pre-climactic surge eruptions, and black = climactic eruption.

magma feeding the dome eruption could have been the same magma drawing up the slowest ascending embayments from their storage region, with the explosive phase resulting in a transition to a faster magma ascent. A similar ‘top-down’ control on magma ascent has been previously speculated for the June 12–14 erupted materials [Hoblitt 1996], meaning that the ascent and eruption of material was driven by a pressure balance from the above plug and feeding magma below. As more magma was input into the system, the decompressing magma eventually exceeded the confining pressure from the shallow plug, and the eruption initiated. The eruption ends once the conduit becomes clogged with pyroclasts, resulting in a confining pressure that exceeds the pressure of the magma supply [Hoblitt 1996]. This process repetitively occurred at shorter intervals leading up to the climactic eruption on June 15 [Hammer et al. 1999]. We thus interpret the ascent of volatile-rich magma in the days leading up to the first explosive eruption on June 12 as exceeding the confining pressure of the overlying andesitic lava dome and clearing the path for subsequent eruptions.

6 CONCLUSION

This study sought to reconcile three common petrologic methods for estimating magma decompression rate to create an integrated model of magma ascent from source to surface, applied to the precursory June 12, 1991, eruption of Mount Pinatubo (Philippines). By applying three updated models that more closely approximate inferred natural magma decompression pathways, this work highlights that melt embayments are a robust tool for restoring magma ascent from stor-

age to surface. The two-stage decompression model applied to embayment volatile gradients resolves an accelerating ascent pathway, where the initial stage of ascent is now in agreement with microlite decompression rates, and the final stage is in agreement with bubble number density decompression rates. Thus, in the event that embayments cannot be found or otherwise leveraged, microlite and bubble number densities may be used together to provide similar information, assuming that the system has not experienced cooling- or flux-driven crystallization. We also find that the two-stage embayment model timescales align well with the extrusion of a lava dome, supporting the model of top-down control on eruptive behavior.

AUTHOR CONTRIBUTIONS

Megan Harris contributed to sample preparation, data collection, modeling, analysis, and manuscript preparation. Behnaz Hosseini contributed to development of the two-stage decompression-diffusion model, modeling, analysis, and manuscript editing. Logan Bouley contributed to thin section preparation, SEM data collection, and analysis. Madison Myers contributed to project conception and funding, sample acquisition and manuscript editing.

ACKNOWLEDGEMENTS

This work was funded by NSF EAR award 1922513 to M. Myers. The authors thank John Pallister and Heather Wright for their thoughtful discussions and comments throughout the duration of this project, and both reviewers for their useful feedback that led to a cleaner presentation of this manuscript.

M. Myers also thanks Chris Newhall and Betchaida Payot for their help planning a COVID-spoiled field excursion.

DATA AVAILABILITY

Full data sets are available in the online supplemental materials. The two-stage decompression-diffusion model used in this study is publicly available and hosted on GitHub and archived on Zenodo (<https://zenodo.org/record/10042159>). **Supplementary Material** is available alongside the online version of this article.

COPYRIGHT NOTICE

© The Author(s) 2024. This article is distributed under the terms of the **Creative Commons Attribution 4.0 International License**, which permits unrestricted use, distribution, and reproduction in any medium, provided you give appropriate credit to the original author(s) and the source, provide a link to the Creative Commons license, and indicate if changes were made.

REFERENCES

- Andrews, B. J. and K. S. Befus (2020). “Supersaturation Nucleation and Growth of Plagioclase: a numerical model of decompression-induced crystallization”. *Contributions to Mineralogy and Petrology* 175(3). DOI: [10.1007/s00410-020-1660-9](https://doi.org/10.1007/s00410-020-1660-9).
- Armienti, P., C. Perinelli, and K. D. Putirka (2013). “A New Model to Estimate Deep-level Magma Ascent Rates, with Applications to Mt. Etna (Sicily, Italy)”. *Journal of Petrology* 54(4), pages 795–813. DOI: [10.1093/petrology/egs085](https://doi.org/10.1093/petrology/egs085).
- Befus, K. S. and B. J. Andrews (2018). “Crystal nucleation and growth produced by continuous decompression of Pinatubo magma”. *Contributions to Mineralogy and Petrology* 173(11). DOI: [10.1007/s00410-018-1519-5](https://doi.org/10.1007/s00410-018-1519-5).
- Befus, K. S., A. C. Ruefer, C. M. Allison, and J. O. Thompson (2023). “Quartz-hosted inclusions and embayments reveal storage, fluxing, and ascent of the Mesa Falls Tuff, Yellowstone”. *Earth and Planetary Science Letters* 601, page 117909. DOI: [10.1016/j.epsl.2022.117909](https://doi.org/10.1016/j.epsl.2022.117909).
- Benage, M. C., H. M. N. Wright, and M. L. Coombs (2021). “Eruption of compositionally heterogeneous andesites from a complex storage region during the 2006 eruption of Augustine Volcano”. *Bulletin of Volcanology* 83(3). DOI: [10.1007/s00445-020-01431-2](https://doi.org/10.1007/s00445-020-01431-2).
- Brandeis, G. and C. Jaupart (1987). “The kinetics of nucleation and crystal growth and scaling laws for magmatic crystallization”. *Contributions to Mineralogy and Petrology* 96(1), pages 24–34. DOI: [10.1007/bf00375522](https://doi.org/10.1007/bf00375522).
- Brugger, C. R. and J. E. Hammer (2010). “Crystallization Kinetics in Continuous Decompression Experiments: Implications for Interpreting Natural Magma Ascent Processes”. *Journal of Petrology* 51(9), pages 1941–1965. DOI: [10.1093/petrology/egq044](https://doi.org/10.1093/petrology/egq044).
- Burgisser, A. and W. Degruyter (2015). “Magma Ascent and Degassing at Shallow Levels”. *The Encyclopedia of Volcanoes*. Edited by H. Sigurdsson. Elsevier, pages 225–236. ISBN: 978-0-12-385938-9. DOI: [10.1016/b978-0-12-385938-9.00011-0](https://doi.org/10.1016/b978-0-12-385938-9.00011-0).
- Cassidy, M., M. Manga, K. Cashman, and O. Bachmann (2018). “Controls on explosive-effusive volcanic eruption styles”. *Nature Communications* 9(1). DOI: [10.1038/s41467-018-05293-3](https://doi.org/10.1038/s41467-018-05293-3).
- Castro, J. M. and J. E. Gardner (2008). “Did magma ascent rate control the explosive-effusive transition at the Inyo volcanic chain, California”. *Geology* 36(4), page 279. DOI: [10.1130/g24453a.1](https://doi.org/10.1130/g24453a.1).
- Eichelberger, J. C. (1995). “Silicic Volcanism: Ascent of Viscous Magmas from Crustal Reservoirs”. *Annual Review of Earth and Planetary Sciences* 23(1), pages 41–63. DOI: [10.1146/annurev.earth.23.050195.000353](https://doi.org/10.1146/annurev.earth.23.050195.000353).
- Georgeais, G., K. T. Koga, Y. Moussallam, and E. F. Rose-Koga (2021). “Magma Decompression Rate Calculations With EMBER: A User-Friendly Software to Model Diffusion of H₂O, CO₂, and S in Melt Embayments”. *Geochemistry, Geophysics, Geosystems* 22(7). DOI: [10.1029/2020gc009542](https://doi.org/10.1029/2020gc009542).
- Gerlach, T. M., H. R. Westrich, and R. B. Symonds (1996). “Preeruption vapor in magma of the climactic Mount Pinatubo eruption: Source of the giant stratospheric sulfur dioxide cloud”. *Fire and mud: eruptions and lahars of Mount Pinatubo, Philippines*. Edited by C. G. Newhall and R. S. Punongbayan. Volume 415. Philippine Institute of Volcanology, Seismology, Quezon City, and University of Washington Press, Seattle, page 33.
- Ghiorso, M. S. and G. A. R. Gualda (2015). “An H₂O–CO₂ mixed fluid saturation model compatible with rhyolite-MELTS”. *Contributions to Mineralogy and Petrology* 169(6). DOI: [10.1007/s00410-015-1141-8](https://doi.org/10.1007/s00410-015-1141-8).
- Gonnermann, H. M. and M. Manga (2007). “The Fluid Mechanics Inside a Volcano”. *Annual Review of Fluid Mechanics* 39(1), pages 321–356. DOI: [10.1146/annurev.fluid.39.050905.110207](https://doi.org/10.1146/annurev.fluid.39.050905.110207).
- Gualda, G. A. R., M. S. Ghiorso, R. V. Lemons, and T. L. Carley (2012). “Rhyolite-MELTS: a Modified Calibration of MELTS Optimized for Silica-rich, Fluid-bearing Magmatic Systems”. *Journal of Petrology* 53(5), pages 875–890. DOI: [10.1093/petrology/egr080](https://doi.org/10.1093/petrology/egr080).
- Hajimirza, S., H. M. Gonnermann, and J. E. Gardner (2021). “Reconciling bubble nucleation in explosive eruptions with geospeedometers”. *Nature Communications* 12(1). DOI: [10.1038/s41467-020-20541-1](https://doi.org/10.1038/s41467-020-20541-1).
- Hajimirza, S., H. M. Gonnermann, J. E. Gardner, and T. Giachetti (2019). “Predicting Homogeneous Bubble Nucleation in Rhyolite”. *Journal of Geophysical Research: Solid Earth* 124(3), pages 2395–2416. DOI: [10.1029/2018jb015891](https://doi.org/10.1029/2018jb015891).
- Hamada, M., D. Laporte, N. Cluzel, K. T. Koga, and T. Kauamoto (2010). “Simulating bubble number density of rhyolitic pumices from Plinian eruptions: constraints from fast decompression experiments”. *Bulletin of Volcanology* 72(6), pages 735–746. DOI: [10.1007/s00445-010-0353-z](https://doi.org/10.1007/s00445-010-0353-z).
- Hammer, J. E., K. V. Cashman, R. P. Hoblitt, and S. Newman (1999). “Degassing and microlite crystallization during pre-climactic events of the 1991 eruption of Mt. Pinatubo, Philippines”. *Bulletin of Volcanology* 60(5), pages 355–380. DOI: [10.1007/s004450050238](https://doi.org/10.1007/s004450050238).

- Hammer, J. E. and M. J. Rutherford (2002). “An experimental study of the kinetics of decompression-induced crystallization in silicic melt”. *Journal of Geophysical Research: Solid Earth* 107(B1). DOI: [10.1029/2001jb000281](https://doi.org/10.1029/2001jb000281).
- Harlow, D. H., J. A. Power, E. P. Laguerta, G. Ambubuyog, R. A. White, and R. P. Hoblitt (1996). “Precursory seismicity and forecasting of the June 15, 1991, eruption of Mount Pinatubo”. *Fire and Mud: eruptions and lahars of Mount Pinatubo, Philippines*. Edited by C. G. Newhall and R. S. Punongbayan. Philippine Institute of Volcanology, Seismology, Quezon City, and University of Washington Press, Seattle, pages 223–247.
- Hoblitt, R. (1996). “The preclimactic eruptions of Mount Pinatubo, June 1991”. *Fire and Mud: eruptions and lahars of Mount Pinatubo, Philippines*. Edited by C. G. Newhall and R. S. Punongbayan. Philippine Institute of Volcanology, Seismology, Quezon City, and University of Washington Press, Seattle, pages 457–511.
- Hosseini, B. (2023). “EDiTS - Embayment Decompression in Two Stages”. *Zenodo*. DOI: [10.5281/zenodo.10042159](https://doi.org/10.5281/zenodo.10042159). [Software].
- Hosseini, B., M. L. Myers, and M. A. Saalfeld (2022). “Reassessing embayment-based magma ascent rates from silicic to intermediate arc eruptions”. *Geological Society of America Abstracts with Programs*. Volume 54. 2. Geological Society of America. DOI: [10.1130/abs/2022cd-373277](https://doi.org/10.1130/abs/2022cd-373277).
- Hosseini, B., M. L. Myers, and J. Watkins (2021). “Stepping it Up: Reevaluating Embayments from Silicic Caldera-Forming Eruptions with a Two-Stage Decompression-Diffusion Model”. *AGU Fall Meeting Abstracts*. Volume 2021, V14A-02, V14A-02.
- Hosseini, B., M. L. Myers, J. M. Watkins, and M. A. Harris (2023). “Are We Recording? Putting Embayment Speedometry to the Test Using High Pressure-Temperature Decompression Experiments”. *Geochemistry, Geophysics, Geosystems* 24(6). DOI: [10.1029/2022gc010770](https://doi.org/10.1029/2022gc010770).
- Hurwitz, S. and O. Navon (1994). “Bubble nucleation in rhyolitic melts: Experiments at high pressure, temperature, and water content”. *Earth and Planetary Science Letters* 122(3–4), pages 267–280. DOI: [10.1016/0012-821x\(94\)90001-9](https://doi.org/10.1016/0012-821x(94)90001-9).
- Leschik, M., G. Heide, G. Frischat, H. Behrens, M. Wiedenbeck, N. Wagner, K. Heide, H. Geißler, and U. Reinholz (2004). “Determination of H₂O and D₂O contents in rhyolitic glasses”. *Physics and Chemistry of Glasses* 45(4), pages 238–251.
- Liu, Y., A. T. Anderson, and C. J. N. Wilson (2007). “Melt pockets in phenocrysts and decompression rates of silicic magmas before fragmentation”. *Journal of Geophysical Research: Solid Earth* 112(B6). DOI: [10.1029/2006jb004500](https://doi.org/10.1029/2006jb004500).
- Liu, Y., Y. Zhang, and H. Behrens (2005). “Solubility of H₂O in rhyolitic melts at low pressures and a new empirical model for mixed H₂O–CO₂ solubility in rhyolitic melts”. *Journal of Volcanology and Geothermal Research* 143(1–3), pages 219–235. DOI: [10.1016/j.jvolgeores.2004.09.019](https://doi.org/10.1016/j.jvolgeores.2004.09.019).
- Lloyd, A. S., P. Ruprecht, E. H. Hauri, W. Rose, H. M. Gonnermann, and T. Plank (2014). “NanoSIMS results from olivine-hosted melt embayments: Magma ascent rate during explosive basaltic eruptions”. *Journal of Volcanology and Geothermal Research* 283, pages 1–18. DOI: [10.1016/j.jvolgeores.2014.06.002](https://doi.org/10.1016/j.jvolgeores.2014.06.002).
- Mangan, M. T., K. V. Cashman, and S. Newman (1993). “Vesiculation of basaltic magma during eruption”. *Geology* 21(2), page 157. DOI: [10.1130/0091-7613\(1993\)021<0157:vobmde>2.3.co;2](https://doi.org/10.1130/0091-7613(1993)021<0157:vobmde>2.3.co;2).
- Massol, H. and T. Koyaguchi (2005). “The effect of magma flow on nucleation of gas bubbles in a volcanic conduit”. *Journal of Volcanology and Geothermal Research* 143(1–3), pages 69–88. DOI: [10.1016/j.jvolgeores.2004.09.011](https://doi.org/10.1016/j.jvolgeores.2004.09.011).
- Mastin, L. G. (2002). “Insights into volcanic conduit flow from an open-source numerical model”. *Geochemistry, Geophysics, Geosystems* 3(7), pages 1–18. DOI: [10.1029/2001gc000192](https://doi.org/10.1029/2001gc000192).
- Moussallam, Y., E. F. Rose-Koga, K. T. Koga, E. Médard, P. Bani, J.-L. Devidal, and D. Tari (2019). “Fast ascent rate during the 2017–2018 Plinian eruption of Ambae (Aoba) volcano: a petrological investigation”. *Contributions to Mineralogy and Petrology* 174(11). DOI: [10.1007/s00410-019-1625-z](https://doi.org/10.1007/s00410-019-1625-z).
- Myers, M. L., T. H. Druitt, F. Schiavi, L. Gurioli, and T. Flaherty (2021). “Evolution of magma decompression and discharge during a Plinian event (Late Bronze-Age eruption, Santorini) from multiple eruption-intensity proxies”. *Bulletin of Volcanology* 83(3). DOI: [10.1007/s00445-021-01438-3](https://doi.org/10.1007/s00445-021-01438-3).
- Myers, M. L., P. J. Wallace, C. J. Wilson, J. M. Watkins, and Y. Liu (2018). “Ascent rates of rhyolitic magma at the onset of three caldera-forming eruptions”. *American Mineralogist* 103(6), pages 952–965. DOI: [10.2138/am-2018-6225](https://doi.org/10.2138/am-2018-6225).
- Newhall, C. G. and R. S. Punongbayan, editors (1996). *Fire and mud: Eruptions and lahars of Mount Pinatubo, Philippines*. Philippine Institute of Volcanology, Seismology, Quezon City, and University of Washington Press, Seattle.
- Newman, S. and J. B. Lowenstern (2002). “VolatileCalc: a silicate melt–H₂O–CO₂ solution model written in Visual Basic for excel”. *Computers & Geosciences* 28(5), pages 597–604. DOI: [10.1016/s0098-3004\(01\)00081-4](https://doi.org/10.1016/s0098-3004(01)00081-4).
- Nicholis, M. and M. Rutherford (2004). “Experimental constraints on magma ascent rate for the Crater Flat volcanic zone hawaiite”. *Geology* 32(6), page 489. DOI: [10.1130/g20324.1](https://doi.org/10.1130/g20324.1).
- Paladio-Melosantos, M. L. O., R. U. Solidum, W. E. Scott, R. B. Quiambao, J. V. Umbal, K. S. Rodolfo, B. S. Tubianosa, P. Delos Reyes, R. A. Alonso, H. B. Ruelo, et al. (1996). “Tephra falls of the 1991 eruptions of Mount Pinatubo”. *Fire and mud: eruptions and lahars of Mount Pinatubo, Philippines*. Edited by C. G. Newhall and R. S. Punongbayan. Philippine Institute of Volcanology, Seismology, Quezon City, and University of Washington Press, Seattle, pages 513–535.

- Pallister, J. S., R. P. Hoblitt, G. P. Meeker, R. J. Knight, D. F. Siems, et al. (1996). "Magma mixing at Mount Pinatubo: petrographic and chemical evidence from the 1991 deposits". *Fire and mud: eruptions and lahars of Mount Pinatubo, Philippines*. Edited by C. G. Newhall and R. S. Punongbayan. Philippine Institute of Volcanology, Seismology, Quezon City, and University of Washington Press, Seattle, pages 687–731.
- Papale, P. and M. Polacci (1999). "Role of carbon dioxide in the dynamics of magma ascent in explosive eruptions". *Bulletin of Volcanology* 60(8), pages 583–594. DOI: [10.1007/s004450050253](https://doi.org/10.1007/s004450050253).
- Polacci, M., P. Papale, and M. Rosi (2001). "Textural heterogeneities in pumices from the climactic eruption of Mount Pinatubo, 15 June 1991, and implications for magma ascent dynamics". *Bulletin of Volcanology* 63(2–3), pages 83–97. DOI: [10.1007/s004450000123](https://doi.org/10.1007/s004450000123).
- Ruefer, A. C., K. S. Befus, J. O. Thompson, and B. J. Andrews (2021). "Implications of Multiple Disequilibrium Textures in Quartz-Hosted Embayments". *Frontiers in Earth Science* 9. DOI: [10.3389/feart.2021.742895](https://doi.org/10.3389/feart.2021.742895).
- Rutherford, M. J. and J. D. Devine (1996). "Preeruption pressure-temperature conditions and volatiles in the 1991 dacitic magma of Mount Pinatubo". *Fire and mud: eruptions and lahars of Mount Pinatubo, Philippines*. Edited by C. G. Newhall and R. S. Punongbayan. Philippine Institute of Volcanology, Seismology, Quezon City, and University of Washington Press, Seattle, pages 751–766.
- Saalfeld, M. A., M. L. Myers, R. deGraffenried, T. Shea, and C. M. Waelkens (2022). "On the rise: using reentrants to extract magma ascent rates in the Bandelier Tuff caldera complex, New Mexico, USA". *Bulletin of Volcanology* 84(1). DOI: [10.1007/s00445-021-01518-4](https://doi.org/10.1007/s00445-021-01518-4).
- Scandone, R. and S. D. Malone (1985). "Magma supply, magma discharge and readjustment of the feeding system of mount St. Helens during 1980". *Journal of Volcanology and Geothermal Research* 23(3–4), pages 239–262. DOI: [10.1016/0377-0273\(85\)90036-8](https://doi.org/10.1016/0377-0273(85)90036-8).
- Shea, T. (2017). "Bubble nucleation in magmas: A dominantly heterogeneous process?" *Journal of Volcanology and Geothermal Research* 343, pages 155–170. DOI: [10.1016/j.jvolgeores.2017.06.025](https://doi.org/10.1016/j.jvolgeores.2017.06.025).
- Shea, T., B. F. Houghton, L. Gurioli, K. V. Cashman, J. E. Hammer, and B. J. Hobden (2010). "Textural studies of vesicles in volcanic rocks: An integrated methodology". *Journal of Volcanology and Geothermal Research* 190(3–4), pages 271–289. DOI: [10.1016/j.jvolgeores.2009.12.003](https://doi.org/10.1016/j.jvolgeores.2009.12.003).
- Skirius, C. M., J. W. Peterson, and A. T. Anderson (1990). "Homogenizing rhyolitic glass inclusions from the Bishop Tuff". *American Mineralogist* 75(11-12), pages 1381–1398.
- Toramaru, A. (2006). "BND (bubble number density) decompression rate meter for explosive volcanic eruptions". *Journal of Volcanology and Geothermal Research* 154(3–4), pages 303–316. DOI: [10.1016/j.jvolgeores.2006.03.027](https://doi.org/10.1016/j.jvolgeores.2006.03.027).
- Toramaru, A., S. Noguchi, S. Oyoshihara, and A. Tsune (2008). "MND(microlite number density) water exsolution rate meter". *Journal of Volcanology and Geothermal Research* 175(1–2), pages 156–167. DOI: [10.1016/j.jvolgeores.2008.03.035](https://doi.org/10.1016/j.jvolgeores.2008.03.035).
- White, J. P. and M.-N. Harris (1997). "Changing sources: early Lapita period obsidian in the Bismarck Archipelago". *Archaeology in Oceania* 32(1), pages 97–107. DOI: [10.1002/j.1834-4453.1997.tb00375.x](https://doi.org/10.1002/j.1834-4453.1997.tb00375.x).
- Wilson, L., R. S. J. Sparks, and G. P. L. Walker (1980). "Explosive volcanic eruptions – IV. The control of magma properties and conduit geometry on eruption column behaviour". *Geophysical Journal International* 63(1), pages 117–148. DOI: [10.1111/j.1365-246x.1980.tb02613.x](https://doi.org/10.1111/j.1365-246x.1980.tb02613.x).
- Wolfe, E. and R. Hoblitt (1996). "Overview of the eruptions". *Fire and mud: eruptions and lahars of Mount Pinatubo, Philippines*. Edited by C. G. Newhall and R. S. Punongbayan. Philippine Institute of Volcanology, Seismology, Quezon City, and University of Washington Press, Seattle.
- Wysoczanski, R. and K. Tani (2006). "Spectroscopic FTIR imaging of water species in silicic volcanic glasses and melt inclusions: An example from the Izu-Bonin arc". *Journal of Volcanology and Geothermal Research* 156(3–4), pages 302–314. DOI: [10.1016/j.jvolgeores.2006.03.024](https://doi.org/10.1016/j.jvolgeores.2006.03.024).
- Zhang, Y., Z. Xu, M. Zhu, and H. Wang (2007). "Silicate melt properties and volcanic eruptions". *Reviews of Geophysics* 45(4). DOI: [10.1029/2006rg000216](https://doi.org/10.1029/2006rg000216).